



A PANN-Based Grid Downscaling Technology and Its Application in Landslide and Flood Modeling

Binlan Zhang ^{1,2} , Chaojun Ouyang ^{2,*} , Dongpo Wang ¹ , Fulei Wang ² and Qingsong Xu ³

¹ State Key Laboratory of Geohazard Prevention and Geoenvironment Protection, Chengdu University of Technology, Chengdu 610059, China; binbinlan@stu.cdut.edu.cn (B.Z.); wangdongpo2014@cdut.edu.cn (D.W.)

² Key Laboratory of Mountain Hazards and Surface Process, Institute of Mountain Hazards and Environment, Chinese Academy of Sciences, Chengdu 610041, China

³ Data Science in Earth Observation, Technical University of Munich, 80333 Munich, Germany; qingsong.xu@tum.de

* Correspondence: cjouyang@imde.ac.cn

Abstract: The efficiency and accuracy of grid-based computational fluid dynamics methods are strongly dependent on the chosen cell size. The computational time increases exponentially with decreasing cell size. Therefore, a grid coarsening technology without apparent precision loss is essential for various numerical modeling methods. In this article, a physical adaption neural network (PANN) is proposed to optimize coarse grid representation from a fine grid. A new convolutional neural network is constructed to achieve a significant reduction in computational cost while maintaining a relatively accurate solution. An application to numerical modeling of dynamic processes in landslides is firstly carried out, and better results are obtained compared to the baseline method. More applications in various flood scenarios in mountainous areas are then analyzed. It is demonstrated that the proposed PANN downscaling method outperforms other currently widely used downscaling methods. The code is publicly available and can be applied broadly. Computing by PANN is hundreds of times more efficient, meaning that it is significant for the numerical modeling of various complicated Earth-surface flows and their applications.

Keywords: physical adaption neural network; numerical modeling; downscaling; landslide; partial differential equations; topography



Citation: Zhang, B.; Ouyang, C.;

Wang, D.; Wang, F.; Xu, Q. A

PANN-Based Grid Downscaling
Technology and Its Application in
Landslide and Flood Modeling.

Remote Sens. **2023**, *15*, 5075. <https://doi.org/10.3390/rs15205075>

Academic Editor: Bruno Adriano

Received: 14 September 2023

Revised: 17 October 2023

Accepted: 19 October 2023

Published: 23 October 2023



Copyright: © 2023 by the authors. Licensee MDPI, Basel, Switzerland. This article is an open access article distributed under the terms and conditions of the Creative Commons Attribution (CC BY) license (<https://creativecommons.org/licenses/by/4.0/>).

1. Introduction

Computational fluid dynamics (CFD) is an effective way to explain natural phenomena; such problems are usually solved numerically, since no closed-form solution is available for most of them [1]. Classical numerical computational methods, such as finite difference, finite volume, finite element, and pseudo-spectral methods [2–4] have been used to obtain great achievements in the simulation of Earth-surface flows, such as landslides, floods, debris flows, avalanches [5,6], etc. Generally, accuracy and efficiency are the two major indicators in evaluating the performance of numerical models. These can be improved by (1) adjusting different terms in the equations to explain the detailed behavior of physical phenomena [7]; (2) adopting different orders of precision to restrict discretization inaccuracy on the premise of ensuring numerical stability [8]; and (3) optimizing the scale and dimensionality of modeling for specific problems [9]. Accuracy and efficiency are often in conflict with each other, and a compromise is commonly sought in practical applications. Much work has been conducted by previous scholars to optimize this problem. In this study, a physical adaption neural network (PANN) focuses on the third aspect above, aiming to simplify the numerical model while preserving computational accuracy.

With rapid developments in surveying in recent decades, techniques such as Light Detection and Ranging (LiDAR) and Interferometric Synthetic Aperture Radar (InSAR) have been adopted to obtain high-resolution digital terrain models (DTMs) and digital

elevation models (DEMs) [10,11]. While utilizing high-resolution digital elevation maps can enhance the accuracy of numerical models, it also comes at the cost of increased computational time. To address this challenge, various computational technologies have been employed to improve solving efficiency. Paralleling skills such as Message Passing Interface (MPI), Open Multi Processing (Open-MP), and Graphical Processing Units (GPUs) have been largely applied to speed up numerical modelling [12,13]. Adaptive mesh refinement (AMR) has also been used to change the grid size in different computational domains, and high-precision solutions have been obtained [14]. In addition, Filelis-Papadopoulos [15] adopted the multigrid (MG) method to effectively improve the convergence speed of an iterative algorithm through conversion between a coarse mesh and a fine mesh. Further, with the advent of the big data era [16], DL methods have also been employed to accelerate CFD simulations. One general idea is to train a neural network to minimize the residual of partial differential equations (PDEs) as a proxy model for solving PDEs [17–19]. However, due to the complexity of nonlinear systems, these DL methods face challenges in generalizing beyond the training domain [20,21].

Grid downscaling is another effective method for accelerating CFD by spatially predicting unknown values from high to low resolution. Traditional downscaling approaches, such as those based on linear, polynomial, spline, and radial basis functions, have been widely used for decades [22–24]. However, these fixed-parameter algorithms often result in severe terrain distortion and inaccurate simulations in practical applications. Recently, convolutional neural networks (CNNs) have stood out among the DL models due to their powerful abilities of local perception, parameter sharing, and representational learning [25,26], but most of the related research has only focused on image recognition, semantic segmentation, or object detection [27]. An innovative and feasible attempt could be made to use CNNs for terrain grid downscaling. Both images and terrain grids are structured data, which inspired us to build a novel CNN model called PANN for terrain grid downscaling to reduce the input error (terrain elevation) to accelerate CFD. Inspired by the 's usage of machine learning [28,29] for flood modeling, we built PANN to optimize coarse grid representation from a fine grid to enable a significant reduction in computational cost, while maintaining an accurate solution. This research demonstrates, for the first time, that PANN learns to downscale effectively from PDEs and has the ability to perceive physical processes in real cases.

2. The Proposed Method

2.1. Overview of the Computational Framework

In this study, we propose a novel downscaling technology, PANN, to learn and retain the physical details from partial differential equations (PDEs) that fit the characteristics of a dynamic process, as shown in Figure 1. **Firstly**, the input fine-grid terrain map is downscaled to a coarse-grid terrain map by PANN. **Next**, identical randomly generated initial and boundary conditions are applied to both terrains multiple times. The utilization of boundary and initial conditions generated by random functions aims to restore the movement and coverage of a variety of fluids in the real world as much as possible. Moreover, this augmentation of datasets helps to mitigate the risk of model overfitting [30]. **Then**, the same numerical solver configuration is used to compute both solutions at the same time steps. **After that**, the difference between the two solutions is calculated through the grid. **Finally**, the PANN is optimized via back propagation to reduce the loss until the model converges [31].

More specifically, the adopted numerical solver is the depth-integrated continuum method (namely, Massflow) [32], which translates the three-dimensional Navier–Stokes (N–S) equations into two-dimensional mass and momentum equations, realizing efficient numerical modeling of the surface dynamic process. In fact, friction terms can also be adjusted to suit different simulated disaster types, and the model can also learn different sampling characteristics through this.

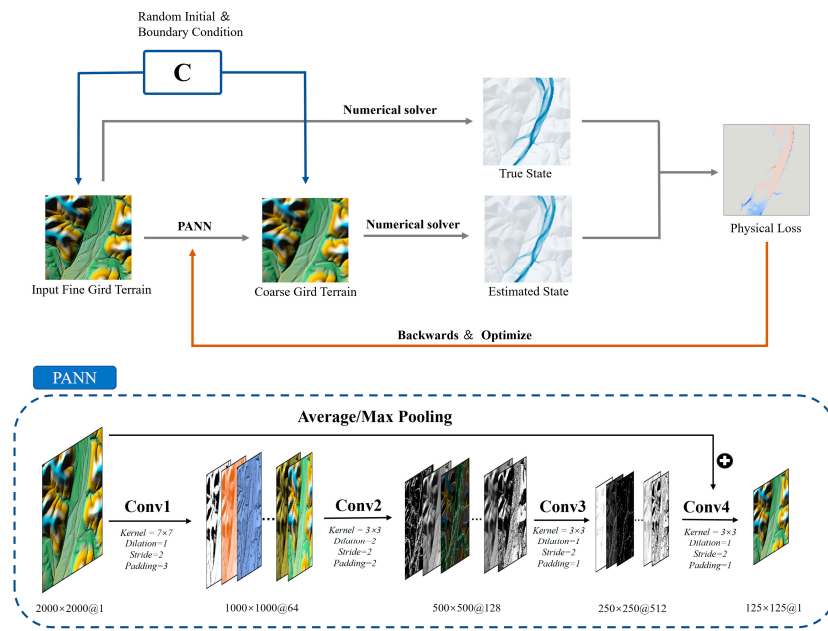


Figure 1. The upper part shows the flow chart of the proposed framework with PANN downscaling technology. Blue arrows represent the pre-process, gray arrows represent the forward propagation process, and the yellow arrow represents back propagation and optimization. The lower part shows the profile of the physical adaption neural network with 16-times downscaling. The downscaling ratio can be changed by adjusting the number of Conv-blocks.

2.2. Physical Adaption Neural Network (PANN)

It has been proved that the convolutional neural network (CNN) has excellent ability in pattern recognition, feature extraction [33,34], etc. As depicted in Figure 1, the designed PANN uses a standard convolutional structure with dilation [35] as its basic unit, and the convolutional parameters are adjusted at different levels to control the output size.

The convolutional input of the PANN convolutional layers is composed of a digital terrain elevation model, with a shape of a 1-channel matrix of size 2000×2000 with 1 m resolution. In the first convolutional layer, a 7×7 convolutional kernel is employed to achieve a larger receptive field, enabling the model to capture more morphological information from the surrounding terrain. For the subsequent convolutional layers, fixed 3×3 convolutional kernels are used to progressively coarsen the grid. Additionally, PANN incorporates average/max pooling in the output layer to fuse more original terrain information. As a result, the final output is a 1-channel coarsened terrain model of size 125×125 with 16 m resolution, downsampled by a factor of 16.

The downscaling ratio can be adjusted according to the needs of the task. For example, for R -dimensional modeling problems, limited by the Courant–Friedrichs–Lewy (CFL) condition, an x^{R+1} -times speedup can be obtained when using an x -times down-sampling ratio [36].

2.3. Numerical Solver with Gradients Retained

The N-S equations are a set of PDEs that can be used to describe the motion of viscous fluid substances. When simulating surface dynamic processes, the N-S equations can be depth-integrated to derive shallow-water equations (Equation (1)).

$$\frac{\partial W}{\partial t} + \frac{\partial F}{\partial x} + \frac{\partial G}{\partial y} = S \quad (1)$$

This is a hyperbolic, nonlinear system composed of mass and momentum conservations PDEs, for which the matrix form can be written as Equation (2). In the formula,

z represents the terrain height, h represents the fluid depth, and u and v represent the velocity of fluid along the x and y axes, respectively.

$$W = \begin{bmatrix} h \\ hu \\ hv \end{bmatrix}, F = \begin{bmatrix} hu \\ hu^2 \\ huv \end{bmatrix}, G = \begin{bmatrix} hv \\ huv \\ hv^2 \end{bmatrix}, S = \begin{bmatrix} 0 \\ -k_x gh \frac{\partial(z+h)}{\partial x} - S_{fx} \\ -k_y gh \frac{\partial(z+h)}{\partial y} - S_{fy} \end{bmatrix} \quad (2)$$

Here, S includes the pressure and bed gradients and friction. The friction term can be chosen to suit the specific fluid properties. Two friction models are considered in this article. For landslides, the Mohr–Coulomb model [37] has been widely adopted, as shown in Equation (3), where δ , c , and ρ refer to the angle of internal friction, cohesion, and fluid density, respectively.

$$S_f = gh \tan(\delta) + \frac{c}{\rho} \quad (3)$$

For floods, it is assumed that the basal resistance of the fluid is only controlled by the surface roughness, and the Manning model is derived as shown in Equation (4), where n is the Manning coefficient.

$$S_f = \frac{gn^2(u^2 + v^2)}{h^{1/3}} \quad (4)$$

Our proposed model, PANN, is named with reference to physical adaption because it preserves gradients and optimizes them adaptively through partial derivatives in the solver. In the numerical scheme, the finite difference method is used to approximate derivatives. Due to the automatic derivation mechanism of the deep learning model, the derivative information about terrain z can be learned by the convolutional filters in PANN, even after thousands of time-step iterations.

2.4. Implementation Details and Optimization

To guarantee a dataset of quality and size suitable for landslide modeling, we chose Gunnison Forest Park (106°33'32.5"W, 38°41'24.2"N; Colorado, USA) with a 1 × 1 m resolution DEM as the training set. According to the landslide inventory provided by the United States Geological Survey (<https://www.usgs.gov/tools/us-landslide-inventory>, accessed on 1 January 2023), this study area is located in the Rocky Mountains, with high landslide susceptibility, and the total coverage area is about 2000 km². (<https://apps.nationalmap.gov/downloader/>, accessed on 1 January 2023). (The optimal experimental parameter configuration was determined through experiments, as detailed in Supplementary Figure S3.)

Due to GPU memory constraints, we cropped the input raster of samples to 2 km × 2 km for a total of 520 samples, using K-fold cross-validation ($k = 3$) [38] to guarantee model generalization, and randomly configured the initial and boundary conditions for them. Specifically, they were divided into three types:

- (1) Inflows and outflows of random rectangle boundaries;
- (2) Random volume sources generated and moved inside the terrain;
- (3) Point source flows generated inside a random upper quartile of the terrain elevation.

3. Results and Discussion

3.1. Model Verification

We used the pre-trained PANN for a case study and analyzed how it learned to downsample adaptively from fine terrain to achieve excellent performance; the results are shown in Figure 2. (A comparison with other methods is shown in Supplementary Figures S1 and S2 and Supplementary Tables S1 and S2.)

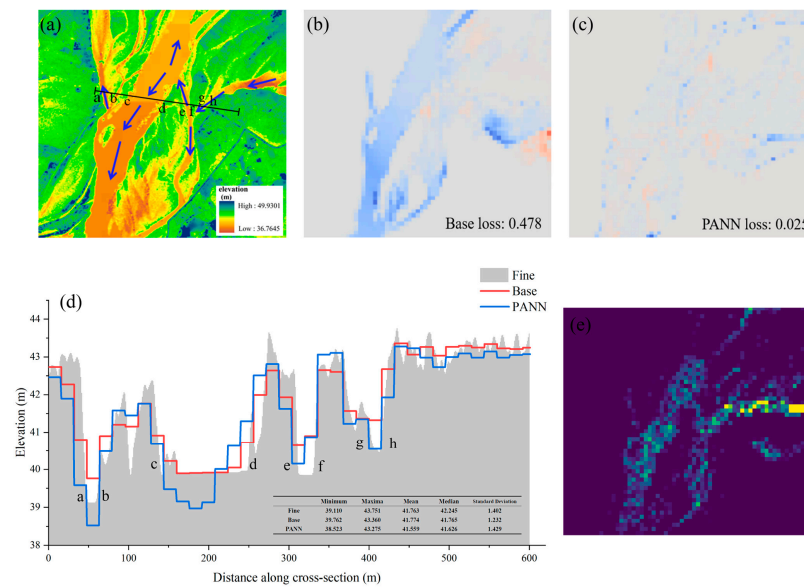


Figure 2. A case where fluid rushes in from the river channel at the right boundary: (a) the digital elevation map, where blue arrows represent the orientation of movement; (b,c) a comparison of difference maps from two methods; (d) a topographic profile cut from (a); (e) the activated heat map of gradients on the terrain through back propagation.

It was assumed that fluid rushes in from the right boundary of the curved channel with a significant elevation difference, as shown in Figure 2a. We utilized both nearest neighbor interpolation as the baseline method and PANN to generate coarse terrain. Subsequently, employing the same numerical scheme, we compared the two results with the fine solution, and the differences are depicted in Figure 2b,c. Blue indicates fluid shallower in the coarse grid, and red indicates fluid deeper in the coarse grid. In terms of error, it was thus demonstrated that PANN outperformed the baseline method completely. In addition, in order to analyze the causes of the differences, we cut a topographic section from Figure 2a and displayed it in Figure 2d.

The a-b, c-d, e-f, g-h are the cross-sections of the channels in the fine grid. In the fine grid (the target we aim to approach), the fluid rushes in from the g-h channel first, then flows into the main channel c-d along the narrow e-f channel, and then flows into the branch a-b due to the difference in gravitational potential energy. However, in the coarse grid from the baseline method, the e-f channel is so narrow that the depth of its terrain was erased in the process of coarsening (it can be seen from Figure 2d that it was lifted by the surrounding terrain elevation by interpolation), causing the channel to behave like a plug, so that most of the fluid could not rush into the c-d and a-b river channels; a large depth error was thus generated. Both the Base and PANN methods exhibited minimal, median, mean, and median sampling errors in the terrain height that did not exceed 2%. In terms of standard deviation, the relative error for the Base method was 12.13%, while for PANN, it was 1.93%. These findings indicate that the terrain distribution achieved by PANN is closer to the fine grid, resulting in smaller terrain changes caused by sampling.

In the coarse grid obtained via the PANN method, PANN cleverly learned the physical details from the characteristics of the dynamic process and selectively changed the depth of channel terrain, so that the fluid could approach the same range and depth as in the fine grid, while in the non-accumulation areas, its terrain was similar to that from the baseline method. To explore its mechanism, we activated the gradient map of the feature layer [39], as shown in Figure 2e. Brighter pixels in the terrain represent larger gradients, and the model tended to prioritize optimization. It can be seen that the gradient information was mainly retained in the region of fluid movements, where it was largest at the inflow g-h channel, indicating that PANN was aware that the entire process was caused by upstream influx. In the non-accumulation areas, the gradient information is close to zero, indicating

that PANN was not interested in these areas; that is, modifying the terrain of these areas would not improve the modeling accuracy. It stands to reason that PANN can approach the fine solution infinitely and globally when we consider sufficient multiple conditions.

3.2. Model Application and Generalization

To assess the model robustness and generalization capacity, several validations using real events were carried out. The Baige landslide was selected as a case study to verify the model with Coulomb friction. Additionally, generalization of the model with Manning friction in flood inundation modeling was examined to evaluate its applicability to different scenarios.

(1) The Baige landslide with the Coulomb friction model

The Baige landslide ($98^{\circ}42'17.98''\text{E}$, $31^{\circ}4'56.41''\text{N}$) occurred twice in total; the first occurrence was on October 11, 2018, when about $24 \times 10^6 \text{ m}^3$ of material failed and rushed into the river, inducing hazard chains [40–42]. After the incident, optical and SAR images were merged to study the deformation characteristics before failure. At the same time, emergency teams went to the site to obtain accurate terrain information based on UAV aerial photogrammetry. Here, we used the resulting 1 m resolution accurate mesh solution as the ground truth to validate the model. We took the terrain sampled by PANN as the surface elevation, and the UAV-based DEMs were used to calculate the landslide volume and simulate its propagation characteristics. Experiments were conducted on Massflow [43], and the corresponding results are presented in Figure 3.

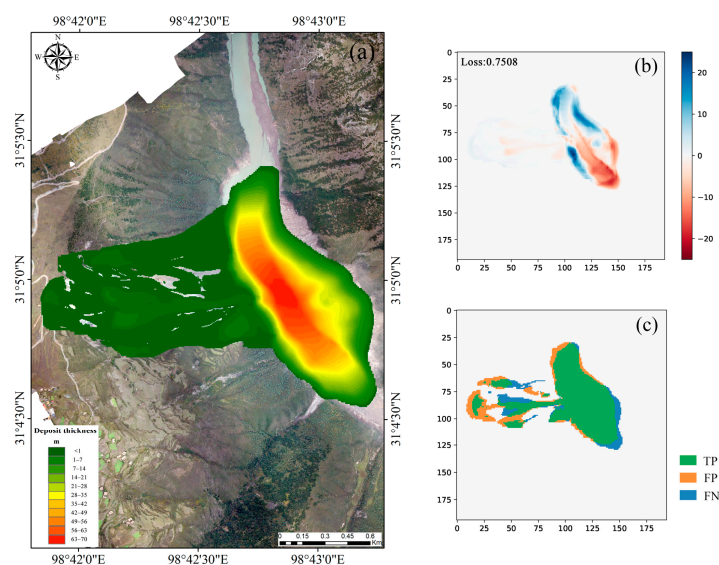


Figure 3. (a) Snapshot of computed flow height contours of the first Baige landslide with fine terrain regarded as ground truth to compare different downscaling models. (b) Difference thickness map of the coarse solution downscaled by PANN. Blue indicates materials more deposited in the coarse grid, and red indicates materials more deposited in the fine grid. (c) Difference category map of the coarse solution downscaled by PANN. Green, yellow, and blue represent true positive, false positive, and false negative, respectively.

It is reasonable to ask whether other downscaling technology can perform better than the baseline but without requiring the heavy machine learning methods. In addition to using the nearest neighbor method as the baseline, we used the two most widely used resampling methods in the ArcMap toolbox for comparison, the Linear and Cubic methods, as shown in Table 1. In the table, Loss represents the average deposit thickness error per grid cell, Precision measures the proportion of true positive samples among the samples, and Recall measures the ability of the model to correctly identify true positive samples, as

shown in Equations (5) and (6). The larger TP, Precision, and Recall are, the better the results are, and vice versa for FP, FN, and Loss (m). Bold font represents the best performance.

Table 1. Comparison of various resampling methods with PANN.

	TP	FP	FN	Loss (m)	Precision	Recall
Base	3859	1287	763	0.868593	0.7500	0.8350
Linear	3824	1264	751	0.864429	0.7516	0.8358
Cubic	3866	1227	784	0.850005	0.7591	0.8314
PANN	4043	1003	744	0.750840	0.8012	0.8446

It should be emphasized the computational time for the fine grid was 18 h 26 min 16 s, while the 16-times coarse solution only took 17 s. Compared with the fine solution, which had huge computational and time costs, the coarse scheme sampled by PANN achieved a hit precision rate of more than 80% at a speedup of 3904 times. Compared with the baseline method, the loss was reduced by 13.56%, and the Accuracy and Recall were improved by 6.83% and 1.15%, respectively. These results indicate that this technology enables rapid and accurate assessment of similar disasters, which is crucial for disaster prevention and post-disaster assistance.

$$\text{Precision} = \frac{TP}{TP + FP} \quad (5)$$

$$\text{Recall} = \frac{TP}{TP + FN} \quad (6)$$

(2) Flood Mapping with the Manning friction model

Compared with landslides, floods have a broader impact and higher frequency, with 1.81 billion people (23% of the world population) directly exposed to 1-in-100-year floods all around the world [44,45]. Flood warning is an effective way to reduce their hazards [46]. For example, the Special Flood Hazard Area (SFHA) program carried out by the Federal Emergency Management Agency (FEMA) realizes flood warning by implementing hydrodynamic inundation models on continental-scale land [47]. However, the vertical accuracy and efficiency of large-scale terrain datasets remain the greatest barrier to obtaining accurate flood inundation projections.

Our technology was used to test the performance of such tasks. The generalization ability of the PANN model with Manning friction on various types of terrain was verified, demonstrating the model's robustness. This included three typical landforms with different Manning coefficients, as referenced from the HEC-RAS manual. In each scenario, the inflow was 100 m³/s steady flow, and the inflow width was set to 100 m. The inundation maps after 1 h are compared in Figures 4–6.

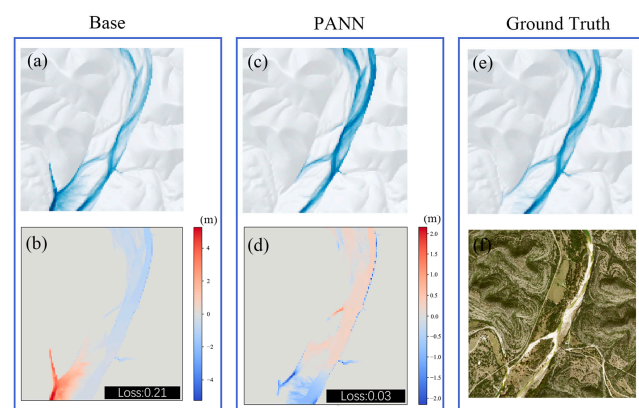


Figure 4. Open ground terrain near the Nueces River, TX, USA. The inflow was set to the upper

results right with a Manning coefficient of 0.15. (a,b) respectively represent the baseline results and difference map, (c,d) respectively represent the PANN and difference map, and (e,f) respectively represent the ground truth and RGB remote sensing images.

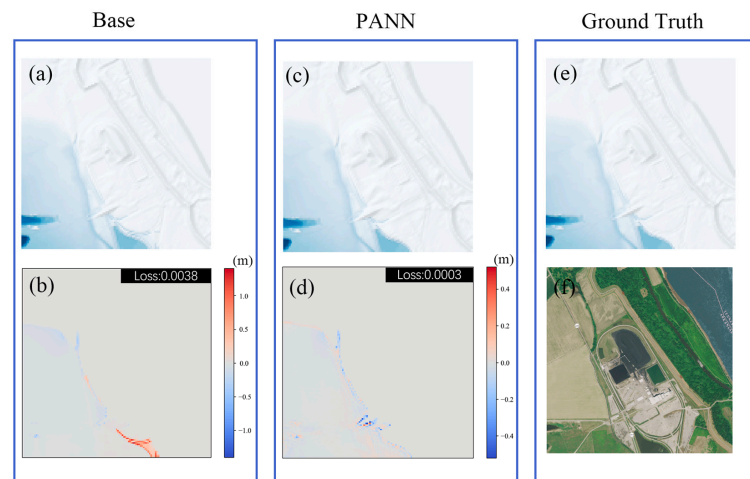


Figure 5. Artificial surface terrain near a factory in Arkansas, AR, USA. The inflow direction was set to the lower left with a Manning coefficient of 0.03. (a,b) respectively represent the baseline results and difference map, (c,d) respectively represent the PANN results and difference map, and (e,f) respectively represent the ground truth and RGB remote sensing images.

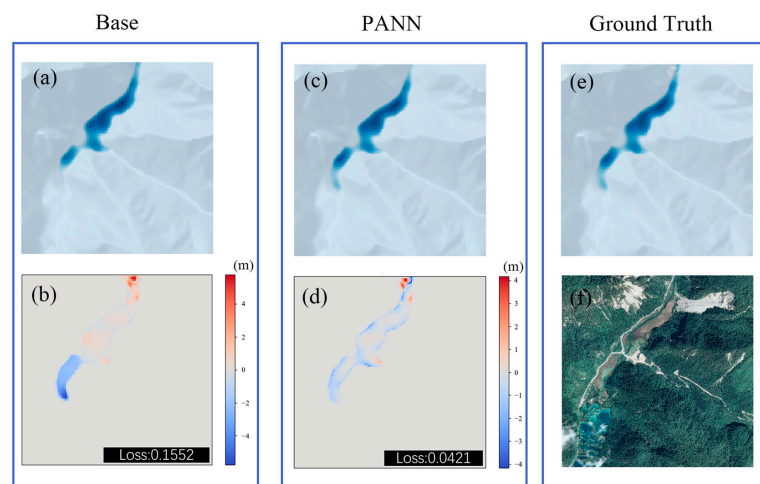


Figure 6. Wet land terrain in Jiuzhaigou, Sichuan, China. The inflow was set to the upper middle with a Manning coefficient of 0.01. (a,b) respectively represent the baseline results and difference map, (c,d) respectively represent the PANN results and difference map, and (e,f) respectively represent the ground truth and RGB remote sensing images.

In Figure 4, the inundation extent of the river in the lower left corner was exaggerated by the baseline method. In Figure 5, the walls outside the factory were smoothed out in the baseline method, resulting in more flooding errors. In Figure 6, the baseline method was unable to correctly represent the distorted river channel, while PANN retained the crucial topographic information that satisfied the hydrological process. The above experiments showed that PANN has better performance in a variety of terrain situations, which makes it possible to generalize physical-process-based adaptive resampling methods on larger-scale datasets in the future.

3.3. Further Discussion

Traditional grid downscaling methods rely on statistical or fixed mathematical algorithms, which do not allow for adaptive optimization as the sample data change [48]. The above experiment proved that the proposed PANN can learn to sample from the physical process, preserving the terrain details that meet the dynamic characteristics to achieve the best performance. (In the cases of landslides and floods, the loss decreased by 13.56% and 59.88%, respectively.) Meanwhile, PANN is easy to deploy for different tasks exclusively. For grids with meter-level resolution, it is recommended to utilize PANN with 16-times downscaling because this rate strikes a favorable balance between efficiency and accuracy. (A sensitivity analysis of the different parameters under various sampling rates can be found in Supplementary Table S3.)

In addition, a robust model should possess continual learning ability. PANN incorporates multiple boundaries and initial conditions during the training process, demonstrating excellent performance even in new scenarios not present in the training set. This robustness demonstrates the global optimization and strong generalization of PANN. Consequently, this technology can further promote the implementation of rapid flood inundation modeling at super-large spatial scales to realize accurate flood forecasting (a 4096-times theoretical speedup with 16-times downscaling), which yields a step forward in our understanding of flood risk management [49].

4. Summary and Conclusions

This research presented the introduction of PANN, a novel grid downscaling technology, aimed at reducing input errors in numerical modeling. PANN adopts a unique approach that combines physics-guided and data-driven schemes for downscaling, surpassing the performance of previous methods. The model's robust generalization capabilities enable accurate disaster modeling, even in new scenarios. Additionally, we verified the effectiveness of PANN with the Coulomb and Manning models, demonstrating that the proposed method can flexibly adjust its learning strategy and sampling rate based on different equation forms, ensuring adherence to physical constraints. Overall, PANN represents a significant advancement in numerical model optimization and holds potential for broader applications in diverse equation forms, which will make it possible to generalize physical-process-based adaptive resampling methods on larger-scale datasets in the future.

Supplementary Materials: The following supporting information can be downloaded at: <https://www.mdpi.com/article/10.3390/rs15205075/s1>, Figure S1: The performance comparison between the Linear interpolation and PANN methods; Figure S2: The performance comparison between the Cubic interpolation and PANN methods; Figure S3: The training process of PANN; Table S1: The elevation analysis of cross-section using Linear and PANN methods.; Table S2: The elevation analysis of cross-section using Cubic and PANN methods. Table S3: Sensitivity analysis results of different parameters. Equations S1 to S3: Three different loss functions tested in this research.

Author Contributions: Conceptualization, C.O.; Methodology, B.Z. and Q.X.; Software, B.Z. and Q.X.; Validation, B.Z., C.O., F.W. and Q.X.; Formal analysis, B.Z. and F.W.; Investigation, Dongpo Wang, F.W. and Q.X.; Resources, C.O. and D.W.; Data curation, F.W.; Writing—original draft, B.Z. and C.O.; Writing—review & editing, C.O. and D.W. All authors have read and agreed to the published version of the manuscript.

Funding: This research was funded by the NSFC (Grant No. 42022054), the Strategic Priority Research Program of CAS (Grant No. XDA23090303), and the Sichuan Science and Technology Program (Grant No. 2022YFS0543, 2022YFG0140).

Data Availability Statement: All codes used for this project are available at this site (<https://github.com/zhang-binlan/pann.git>, accessed on 1 January 2023).

Conflicts of Interest: The authors declared that they have no conflict of interest in this work.

References

1. Blazek, J. *Computational Fluid Dynamics: Principles and Applications*; Butterworth-Heinemann: Oxford, UK, 2015.
2. Bhatti, M.M.; Marin, M.; Zeeshan, A.; Abdelsalam, S.I. Editorial: Recent Trends in Computational Fluid Dynamics. *Front. Phys.* **2020**, *8*, 593111. [[CrossRef](#)]
3. Kochkov, D.; Smith, J.A.; Alieva, A.; Wang, Q.; Brenner, M.P.; Hoyer, S. Machine learning-accelerated computational fluid dynamics. *Proc. Natl. Acad. Sci. USA* **2021**, *118*, e2101784118. [[CrossRef](#)] [[PubMed](#)]
4. Sreirekha, A.; Bassetty, K. Infinite to finite: An overview of finite element analysis. *Indian J. Dent. Res. Off. Publ. Indian Soc. Dent. Res.* **2010**, *21*, 425–432. [[CrossRef](#)] [[PubMed](#)]
5. Fan, T.-Z.; An, H.-C.; Ouyang, C.-J.; Wang, D.-P. Rock characteristics and dynamic fragmentation process of the 2018 Daanshan rockslide in Beijing, China. *J. Mt. Sci.* **2023**, *20*, 448–465. [[CrossRef](#)]
6. Ouyang, C.; Xiang, W.; An, H.; Wang, F.; Yang, W.; Fan, J. Mechanistic Analysis and Numerical Simulation of the 2021 Post-Fire Debris Flow in Xiangjiao Catchment, China. *J. Geophys. Res. Earth Surf.* **2023**, *128*, e2022JF006846. [[CrossRef](#)]
7. Liu, W.; Röckner, M. *Stochastic Partial Differential Equations: An Introduction, Universitext*; Springer: Cham, Switzerland, 2015. [[CrossRef](#)]
8. Goloviznin, V.M.; Chetverushkin, B.N. New Generation Algorithms for Computational Fluid Dynamics. *Comput. Math. Math. Phys.* **2018**, *58*, 1217–1225. [[CrossRef](#)]
9. Lintermann, A. Computational Meshing for CFD Simulations. In *Clinical and Biomedical Engineering in the Human Nose*; Springer: Singapore, 2021; pp. 85–115. [[CrossRef](#)]
10. Haugerud, R.A.; Harding, D.J.; Johnson, S.Y.; Harless, J.L.; Weaver, C.S.; Sherrod, B.L. High-Resolution Lidar Topography of the Puget Lowland, Washington—A Bonanza for Earth Science. *GSA Today* **2003**, *13*, 4. [[CrossRef](#)]
11. Krishnan, S.; Crosby, C.; Nandigam, V.; Phan, M.; Cowart, C.; Baru, C.; Arrowsmith, R. OpenTopography: A services oriented architecture for community access to LIDAR topography. In Proceedings of the 2nd International Conference on Computing for Geospatial Research & Applications—COM.Geo '11, Washington, DC, USA, 23–25 May 2011; ACM Press: Washington, DC, USA, 2011; pp. 1–8. [[CrossRef](#)]
12. Hankin, B.; Waller, S.; Astle, G.; Kellagher, R. Mapping space for water: Screening for urban flash flooding: Mapping space for water. *J. Flood Risk Manag.* **2008**, *1*, 13–22. [[CrossRef](#)]
13. Neal, J.C.; Fewtrell, T.J.; Bates, P.D.; Wright, N.G. A comparison of three parallelisation methods for 2D flood inundation models. *Environ. Model. Softw.* **2010**, *25*, 398–411. [[CrossRef](#)]
14. Diachin, L.F.; Hornung, R.; Plassmann, P.; Wissink, A. Parallel Adaptive Mesh Refinement. In *Parallel Processing for Scientific Computing*; Heroux, M.A., Raghavan, P., Simon, H.D., Eds.; Society for Industrial and Applied Mathematics: Philadelphia, PA, USA, 2006; Volume 8, pp. 143–162. [[CrossRef](#)]
15. Filelis-Papadopoulos, C.K.; Gravvanis, G.A. On the Multigrid Method Based on Finite Difference Approximate Inverses. *Comput. Model. Eng. Sci.* **2013**, *90*, 233–253.
16. Cai, L.; Zhu, Y. The Challenges of Data Quality and Data Quality Assessment in the Big Data Era. *Data Sci. J.* **2015**, *14*, 2. [[CrossRef](#)]
17. Forghani, M.; Qian, Y.; Lee, J.; Farthing, M.W.; Hesser, T.; Kitanidis, P.K.; Darve, E.F. Deep learning-based fast solver of the shallow water equations. *arXiv* **2021**, arXiv:2111.11702.
18. Karniadakis, G.E.; Kevrekidis, I.G.; Lu, L.; Perdikaris, P.; Wang, S.; Yang, L. Physics-informed machine learning. *Nat. Rev. Phys.* **2021**, *3*, 422–440. [[CrossRef](#)]
19. Lu, L.; Meng, X.; Mao, Z.; Karniadakis, G.E. DeepXDE: A Deep Learning Library for Solving Differential Equations. *SIAM Rev.* **2021**, *63*, 208–228. [[CrossRef](#)]
20. Sun, L.; Gao, H.; Pan, S.; Wang, J.-X. Surrogate modeling for fluid flows based on physics-constrained deep learning without simulation data. *Comput. Methods Appl. Mech. Eng.* **2020**, *361*, 112732. [[CrossRef](#)]
21. Hutter, F.; Kothhoff, L.; Vanschoren, J. (Eds.) *Automated Machine Learning: Methods, Systems, Challenges*; Springer: Berlin/Heidelberg, Germany, 2019. [[CrossRef](#)]
22. Aguilar, F.J.; Agüera, F.; Aguilar, M.A.; Carvajal, F. Effects of Terrain Morphology, Sampling Density, and Interpolation Methods on Grid DEM Accuracy. *Photogramm. Eng. Remote Sens.* **2005**, *71*, 805–816. [[CrossRef](#)]
23. Sharifi, E.; Saghafian, B.; Steinacker, R. Downscaling satellite precipitation estimates with multiple linear regression, artificial neural networks, and spline interpolation techniques. *J. Geophys. Res. Atmos.* **2019**, *124*, 789–805. [[CrossRef](#)]
24. Wing, O.E.J.; Bates, P.D.; Neal, J.C.; Sampson, C.C.; Smith, A.M.; Quinn, N.; Shustikova, I.; Domeneghetti, A.; Gilles, D.W.; Goska, R.; et al. A New Automated Method for Improved Flood Defense Representation in Large-Scale Hydraulic Models. *Water Resour. Res.* **2019**, *55*, 11007–11034. [[CrossRef](#)]
25. Reichstein, M.; Camps-Valls, G.; Stevens, B.; Jung, M.; Denzler, J.; Carvalhais, N.; Prabhat. Deep learning and process understanding for data-driven Earth system science. *Nature* **2019**, *566*, 195–204. [[CrossRef](#)]
26. Xu, Q.; Shi, Y.; Bamber, J.; Tuo, Y.; Ludwig, R.; Zhu, X.X. Physics-aware Machine Learning Revolutionizes Scientific Paradigm for Machine Learning and Process-based Hydrology. *arXiv* **2023**, arXiv:2310.05227.
27. Xu, Y.; Liu, X.; Cao, X.; Huang, C.; Liu, E.; Qian, S.; Liu, X.; Wu, Y.; Dong, F.; Qiu, C.-W.; et al. Artificial intelligence: A powerful paradigm for scientific research. *Innovation* **2021**, *2*, 100179. [[CrossRef](#)]

28. Giladi, N.; Ben-Haim, Z.; Nevo, S.; Matias, Y.; Soudry, D. Physics-Aware Downsampling with Deep Learning for Scalable Flood Modeling. *Adv. Neural Inf. Process. Syst.* **2021**, *34*, 1378–1389.
29. Nevo, S.; Morin, E.; Rosenthal, A.G.; Metzger, A.; Barshai, C.; Weitzner, D.; Voloshin, D.; Kratzert, F.; Elidan, G.; Dror, G.; et al. Flood forecasting with machine learning models in an operational framework. *Hydrol. Earth Syst. Sci.* **2022**, *26*, 4013–4032. [[CrossRef](#)]
30. Sun, C.; Shrivastava, A.; Singh, S.; Gupta, A. Revisiting unreasonable effectiveness of data in deep learning era. In Proceedings of the 2017 IEEE International Conference on Computer Vision (ICCV), Venice, Italy, 22–29 October 2017; pp. 843–852.
31. Goh, A.T.C. Back-propagation neural networks for modeling complex systems. *Artif. Intell. Eng.* **1995**, *9*, 143–151. [[CrossRef](#)]
32. Ouyang, C.; He, S.; Xu, Q.; Luo, Y.; Zhang, W. A MacCormack-TVD finite difference method to simulate the mass flow in mountainous terrain with variable computational domain. *Comput. Geosci.* **2013**, *52*, 1–10. [[CrossRef](#)]
33. Shrestha, A.; Mahmood, A. Review of Deep Learning Algorithms and Architectures. *IEEE Access* **2019**, *7*, 53040–53065. [[CrossRef](#)]
34. Xu, Q.; Ouyang, C.; Jiang, T.; Yuan, X.; Fan, X.; Cheng, D. MFFENet and ADANet: A robust deep transfer learning method and its application in high precision and fast cross-scene recognition of earthquake-induced landslides. *Landslides* **2022**, *19*, 1617–1647. [[CrossRef](#)]
35. He, K.; Zhang, X.; Ren, S.; Sun, J. Deep residual learning for image recognition. In Proceedings of the IEEE Computer Society Conference on Computer Vision and Pattern Recognition (CVPR), Las Vegas, NV, USA, 27–30 June 2016; pp. 770–778. [[CrossRef](#)]
36. Gnedin, N.Y.; Semenov, V.A.; Kravtsov, A.V. Enforcing the Courant–Friedrichs–Lewy condition in explicitly conservative local time stepping schemes. *J. Comput. Phys.* **2018**, *359*, 93–105. [[CrossRef](#)]
37. Labuz, J.F.; Zang, A. Mohr–Coulomb Failure Criterion. *Rock Mech. Rock Eng.* **2012**, *45*, 975–979. [[CrossRef](#)]
38. Jung, Y.; Hu, J. AK-fold averaging cross-validation procedure. *J. Nonparametric Stat.* **2015**, *27*, 167–179. [[CrossRef](#)]
39. Selvaraju, R.R.; Cogswell, M.; Das, A.; Vedantam, R.; Parikh, D.; Batra, D. Grad-CAM: Visual Explanations from Deep Networks via Gradient-Based Localization. *Int. J. Comput. Vis.* **2020**, *128*, 336–359. [[CrossRef](#)]
40. An, H.; Ouyang, C.; Zhou, S. Dynamic process analysis of the Baige landslide by the combination of DEM and long-period seismic waves. *Landslides* **2021**, *18*, 1625–1639. [[CrossRef](#)]
41. Bao, Y.; Su, L.; Chen, J.; Ouyang, C.; Yang, T.; Lei, Z.; Li, Z. Dynamic process of a high-level landslide blocking river event in a deep valley area based on FDEM-SPH coupling approach. *Eng. Geol.* **2023**, *319*, 107108. [[CrossRef](#)]
42. Ouyang, C.; An, H.; Zhou, S.; Wang, Z.; Su, P.; Wang, D.; Cheng, D.; She, J. Insights from the failure and dynamic characteristics of two sequential landslides at Baige village along the Jinsha River, China. *Landslides* **2019**, *16*, 1397–1414. [[CrossRef](#)]
43. Ouyang, C.; Zhao, W.; An, H.; Zhou, S.; Wang, D.; Xu, Q.; Li, W.; Peng, D. Early identification and dynamic processes of ridge-top rockslides: Implications from the Su Village landslide in Suichang County, Zhejiang Province, China. *Landslides* **2019**, *16*, 799–813. [[CrossRef](#)]
44. Wei, K.; Ouyang, C.; Duan, H.; Li, Y.; Chen, M.; Ma, J.; An, H.; Zhou, S. Reflections on the Catastrophic 2020 Yangtze River Basin Flooding in Southern China. *Innov.* **2020**, *1*, 100038. [[CrossRef](#)] [[PubMed](#)]
45. Rentschler, J.; Salhab, M.; Jafino, B.A. Flood exposure and poverty in 188 countries. *Nat. Commun.* **2022**, *13*, 3527. [[CrossRef](#)]
46. Harindintwali, J.D.; Wei, K.; Shan, Y.; Mi, Z.; Costello, M.J.; Grunwald, S.; Feng, Z.; Wang, F.; Guo, Y.; Wu, X.; et al. Climate change: Strategies for mitigation and adaptation. *Innov. Geosci.* **2023**, *1*, 100015–1–100015–35. [[CrossRef](#)]
47. Wing, O.E.J.; Bates, P.D.; Sampson, C.C.; Smith, A.M.; Johnson, K.A.; Erickson, T.A. Validation of a 30 m resolution flood hazard model of the conterminous United States: 30 m Resolution flood model of conus. *Water Resour. Res.* **2017**, *53*, 7968–7986. [[CrossRef](#)]
48. Alim, U.R.; Oliveira, T.V.D. A Quality-Preserving Cartesian to Body-Centered Cubic Downsampling Transform. In *EuroVis (Short Papers)*; 2015; 5p. [[CrossRef](#)]
49. Zheng, X.; Maidment, D.R.; Tarboton, D.G.; Liu, Y.Y.; Passalacqua, P. GeoFlood: Large-Scale Flood Inundation Mapping Based on High-Resolution Terrain Analysis. *Water Resour. Res.* **2018**, *54*, 10013–10033. [[CrossRef](#)]

Disclaimer/Publisher’s Note: The statements, opinions and data contained in all publications are solely those of the individual author(s) and contributor(s) and not of MDPI and/or the editor(s). MDPI and/or the editor(s) disclaim responsibility for any injury to people or property resulting from any ideas, methods, instructions or products referred to in the content.